Materials Today Bio 13 (2022) 100188

Contents lists available at ScienceDirect

Materials Today Bio

journal homepage: www.journals.elsevier.com/materials-today-bio

3D-bioprinted peptide coupling patches for wound healing

Gaopeng Guan [a], Qizhuang Lv [b,*], Shengyuan Liu [c], Zhenzhen Jiang [a], Chunxia Zhou [a,**], Weifang Liao [a,***]

[a] Clinical Medical College Jiujiang University Hospital, Jiujiang University, Jiujiang, 332000, Jiangxi, China
[b] College of Biology & Pharmacy, Yulin Normal University, Yulin, 537000, Guangxi, China
[c] Longyan People Hospital of Fujian, Pneumology Department, Longlan, 361000, Fujian, China

ARTICLE INFO

Keywords:
3D-printing
Peptide
Gelatin methacryloyl (GelMA)
Hyaluronic acid methacryloyl (HAMA)
Angiogenesis
Wound healing

ABSTRACT

Chronic wounds caused by severe trauma remain a serious challenge for clinical treatment. In this study, we developed a novel angiogenic 3D-bioprinted peptide patch to improve skin wound healing. The 3D-bioprinted technology can fabricate individual patches according to the shape characteristics of the damaged tissue. Gelatin methacryloyl (GelMA) and hyaluronic acid methacryloyl (HAMA) have excellent biocompatibility and biodegradability, and were used as a biomaterial to produce bioprinted patches. The pro-angiogenic QHREDGS peptide was covalently conjugated to the 3D-bioprinted GelMA/HAMA patches, extending the release of QHREDGS and improving the angiogenic properties of the patch. Our results demonstrated that these 3D-bioprinted peptide patches showed excellent biocompatibility, angiogenesis, and tissue repair both *in vivo* and *in vitro*. These findings indicated that 3D-bioprinted peptide patches improved skin wound healing and could be used in other tissue engineering applications.

1. Introduction

The skin, the largest and outermost organ in the body, plays a vital role in providing a barrier to defend the human body against the outside environment and exogenous stresses [1]. This makes it susceptible to different types of damage, such as burns and wounds. Skin wound healing requires the body to seal and repair the skin defect, a set of complex and dynamic biological processes that involve a coordinated network of cellular responses, extracellular matrix responses, and growth factor action [2]. Generally, based on the self-healing properties of the skin, the wound can be repaired by dressing change, keeping the area clean, and preventing infection. However, particularly large injuries and chronic wounds are often difficult to heal, which imposes enormous economic and psychological burdens for patients and their families [3]. Therefore, improving skin healing remains a considerable challenge of global medical importance [4,5].

Tissue engineering is the application of biomaterials technologies for developing tissue substitutes *in vitro* to restore the function of defective tissues or organs [6]. 3D biological printing is a promising tissue engineering technique that enables the creation of individual, tailor-made patches according to the structural characteristics of the damaged tissue by generating a three-dimensional architecture from a digital model [7]. It leads to the time- and cost-efficient fabrication of custom-engineered products [8]. An appropriate bioink is particularly critical for fabricating 3D-printed patches: it needs to be highly biocompatible, mechanically stable, and have high-shape fidelity post-printing [9]. Gelatin methacryloyl (GelMA) and hyaluronic acid methacryloyl (HAMA) are natural materials (gelatin and hyaluronic acid) with excellent biocompatibility, biodegradability, and biological activity, and have been widely used for 3D printing due to their photo-crosslinking ability and printability [10,11] Therefore, GelMA/HAMA, the compounds derived from the naturally occurring extracellular matrix components, were selected as a biomaterial for patch generation.

Angiogenesis is a critical event that allows the transport and delivery of nutrients and oxygen to prevent hypoxia or metabolite accumulation [12,13]. Angiogenesis is initiated by a local secretion of pro-angiogenic growth factors, such as vascular endothelial growth factors (VEGF) and fibroblast growth factors (FGFs), which, in turn, bind to their cognate receptors on endothelial cells to facilitate endothelial migration, proliferation, and differentiation [14,15]. However, these growth factors have

* Corresponding author.
** Corresponding author.
*** Corresponding author.
E-mail addresses: lvqizhuang062@163.com (Qizhuang Lv), chunxia101636@163.com (C. Zhou), 119007565@qq.com (W. Liao).

https://doi.org/10.1016/j.mtbio.2021.100188
Received 16 October 2021; Received in revised form 6 December 2021; Accepted 10 December 2021
Available online 11 December 2021

several limitations for practical applications, which should not be ignored, such as complicated preparation processes, high cost, short half-life, and antigenicity. Peptides, short amino acid fragments, have gained preference over proteins due to their easy synthesis, better stability, and therapeutic efficiency, offering the possibility of addressing the above-mentioned problems [16–18]. For example, QHREDGS, a novel pro-angiogenic peptide, has the potential to promote skin wound healing [19]. However, these peptides have a serious limitation: they are released too quickly to achieve therapeutic effect when they are applied to skin patches. Therefore, extended peptide release is key to promoting wound healing [20].

Previous studies have reported that 3D-bioprinted pro-angiogenic peptide hydrogel patches have beneficial effects on skin wound healing, exhibiting excellent printability and angiogenic ability [21,22]. However, these 3D-bioprinted peptide patches have several limitations, such as peptide loading and release, which were unsatisfactory. In this study, we improved peptide-loading technology using a chemical coupling method. As shown in Fig. 1, here we fabricated 3D-bioprinted pro-angiogenic peptide-coupled GelMA/HAMA patches for wound healing. These peptide-coupled patches prolong QHREDGS release and provide the patch with angiogenic ability, which would further promote wound healing. Furthermore, GelMA and HAMA, derived from the compounds naturally found in the body, were selected as biomaterials for patch generation and showed excellent biocompatibility and printability. These properties indicated that QHREDGS-conjugated 3D-printed GelMA/HAMA patches could be used for the treatment of skin wounds in a more affordable, effective, and personalized way.

2. Results and discussion

2.1. Fabrication and characterization of the 3D-printed peptide patches

In skin tissue engineering, the mechanical properties of hydrogels need to correspond to the mechanical environment of the surrounding tissue. The main limitation of GelMA for scaffolding is its mechanical strength. Several studies have shown that 15% GelMA has higher mechanical strength than 5% or 10% GelMA [23–25], while 20% GelMA is too viscous and too difficult to handle [25]. At the same time, the Young's modulus of 15% GelMA is about 10 kPa [26], and its mechanical properties are weaker than those of native skin tissues [27]. To overcome this limitation, hybrid GelMA/HAMA hydrogels were fabricated, demonstrating improved physical properties [28]. Furthermore, in mixed GelMA hydrogels, 5% HAMA showed increased mechanical strength compared to 1% HAMA [28]. Therefore, in subsequent experiments, 15% GelMA and 5% HAMA were used.

A schematic diagram of gelatin and hyaluronic acid modification with methacryloyl is presented in Supplementary Fig. S1. 3D-printed patches were photo-crosslinked using ultraviolet (UV) light and then characterized by optical microscopy (Fig. 2A and B) and scanning electron microscopy (SEM) (Fig. 2C and D). Optical microscopy showed that the 3D-printed patches had a well-defined lattice structure (Fig. 2A and B), while SEM confirmed the patch microstructure and morphology: sponge-like structures with surface pores randomly distributed throughout the patches (Fig. 2C and D). The SEM image of the patch fracture surface section also showed a porous structure (Fig. S2). Biodegradability is a fundamental parameter for the application of 3D-printed hydrogel patches to skin wounds. Therefore, we evaluated the biodegradability of hydrogel patches by incubating in collagenase type II solution (2 U/ml) in PBS. Our results showed that the degradation rate of the hydrogel patches was approximately 51.4% at 7-day time point (Fig. S3), indicating a good biodegradability of the 3D-printed hydrogel patches.

2.2. Peptide delivery of the 3D-printed patches in vitro

The FITC-peptide were used as markers for peptide release assays [29]. The lyophilized thin filament patches were loaded with FITC-peptide using chemical coupling. Next, these 3D-printed patches loaded with FITC-peptide were incubated in 100 ml PBS at 37 °C, and the peptide release at different time points was observed by fluorescence microscopy. Fluorescence images showed that green fluorescence was evenly distributed across all patches, confirming that peptides could be loaded into the patches (Fig. S4A). To further characterize FITC-peptide release, fluorescence images were obtained on days 0, 3, 6, 9, 12, and 15. The results demonstrated that the fluorescence intensity of the 3D-printed patches loaded with FITC-peptide using chemical coupling gradually decreased with time upon exposure to PBS (Fig. S4B).

Next, we explored the effect of different filament thickness and different methods of peptide loading on the release of peptides.

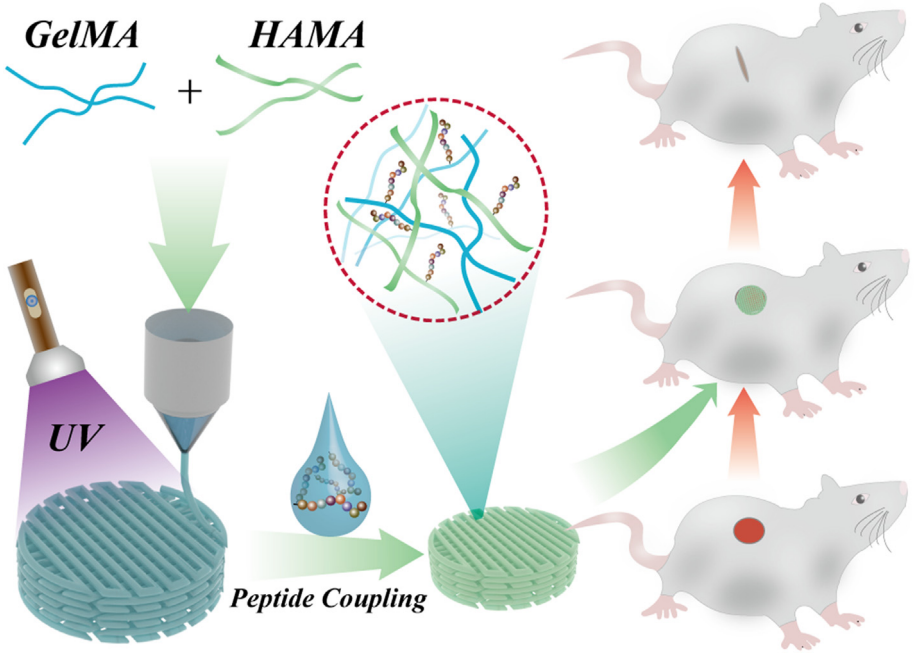

Fig. 1. Schematic diagram of 3D-printed peptide patches fabrication for skin wound therapy.

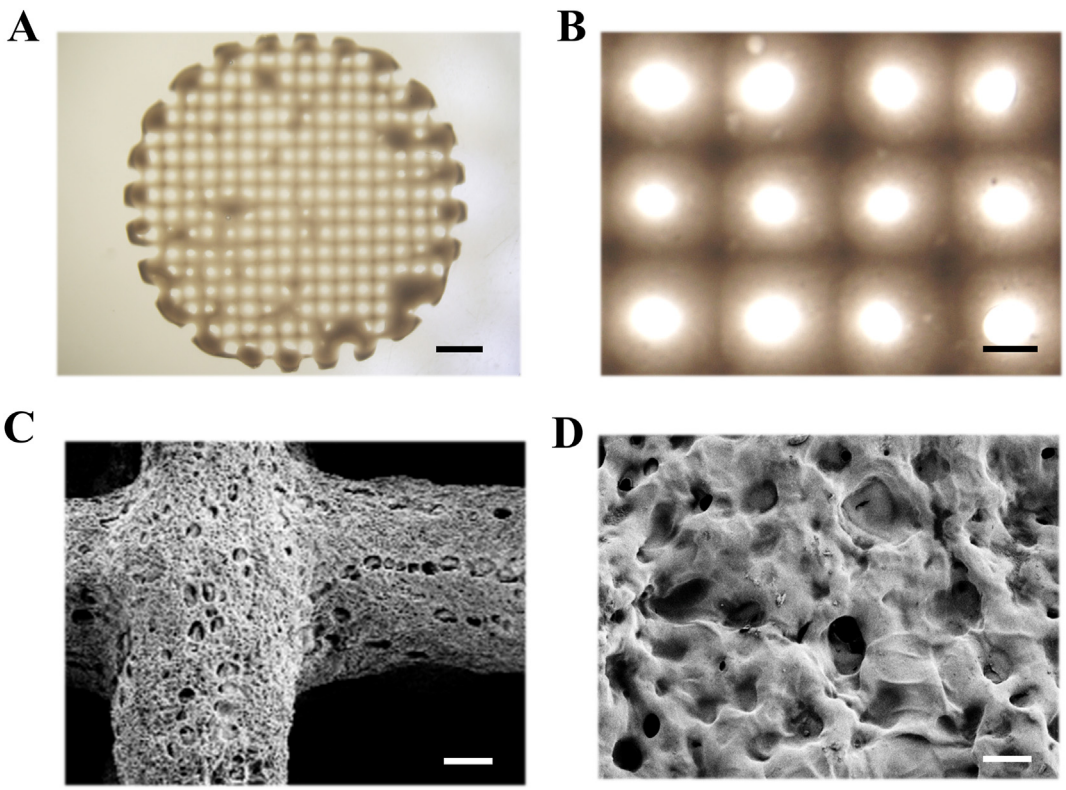

Fig. 2. Characterization of the 3D-printed GelMA/HAMA patches. (A) digital photograph of the 3D-printed GelMA/HAMA patches; (B) micrograph of the 3D-printed GelMA/HAMA patches; (C) SEM image of the 3D-printed GelMA/HAMA patches; (D) magnified SEM image of the surface of 3D-printed GelMA/HAMA patches. The scale bars are 2 mm in (A), 400 μm in (B), 100 μm in (C), and 10 μm in (D).

Lyophilized thin or thick filament patches were loaded with FITC-peptide by chemical coupling or physical absorption. The results indicated that the fluorescence intensity of thin filament patches was weaker, and decay was faster compared to thick filament patches with time in physical absorption-loaded samples (Fig. 3). This is possibly due to the bigger surface of thin filament patches, resulting in faster release. However, the fluorescence intensity was not significantly different between the thin filament patches and thick filament patches in the chemical coupling method (Fig. 3). This could be due to the tighter link of covalent bonds between the FITC-peptide and hydrogels compared to physical absorption. Moreover, the 3D-printed patches loaded with FITC-peptide using physical absorption showed a rapid decline of fluorescence intensity during the initial days (Fig. 3). These results indicated that the 3D-printed patches loaded with FITC-peptide using chemical coupling have a much better drug release ability compared to physical absorption. Therefore, thin filament patches were used in subsequent experiments.

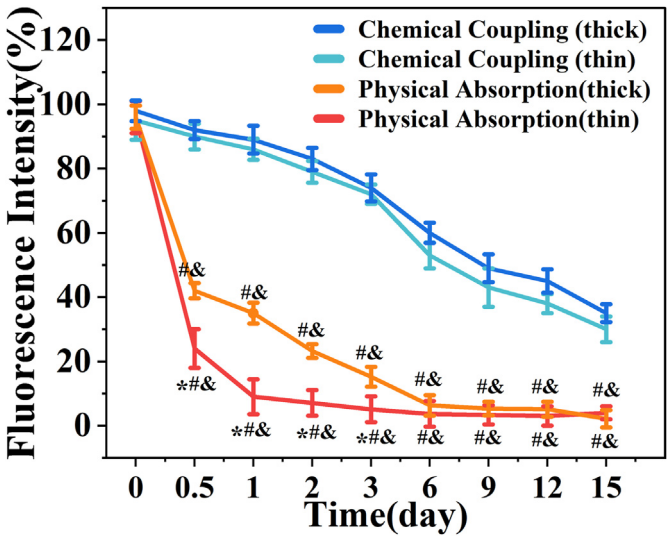

Fig. 3. Peptide release assays. Fluorescent intensity of 3D-printed loading FITC-peptide patches in different filament thickness and different methods of peptide loading. Statistical analysis is shown on the bar graphs. Data are presented as the mean ± SD of the three independent experiments. *P < 0.05 versus Physical Absorption (thick) group; #P < 0.05 versus Chemical Coupling (thin) group; & P < 0.05 versus Chemical Coupling (thick) group.

2.3. Cytocompatibility of the 3D-printed patches in vitro

To evaluate the biocompatibility and biosafety of the 3D-printed patches, human dermal fibroblasts (HDFs) were divided into four groups and treated with PBS (control group), the soaked solution of 3D-printed patches (patch group), QHREDGS solution (peptide group), and the soaked solution of 3D-printed peptide patches (patch & peptide group) for 48 h. Calcein acetoxymethylester/propidium iodide (Calcein-AM/PI) staining and CCK-8 assay were used to evaluate the compatibility of the 3D-printed patches. In the Calcein-AM/PI staining assay, dead or dying cells were stained red by PI, while the live cells were stained green by Calcein-AM. The fluorescent images did not show any obvious morphological abnormalities, and there were no significant differences in the red fluorescence (dead cells) ratio between the groups (Fig. 4A and B). Furthermore, there were no obvious differences in cell proliferation rates after 48 h of culture as determined by the CCK-8 assay (Fig. 4C). These results suggested that the 3D-printed patches showed excellent biocompatibility.

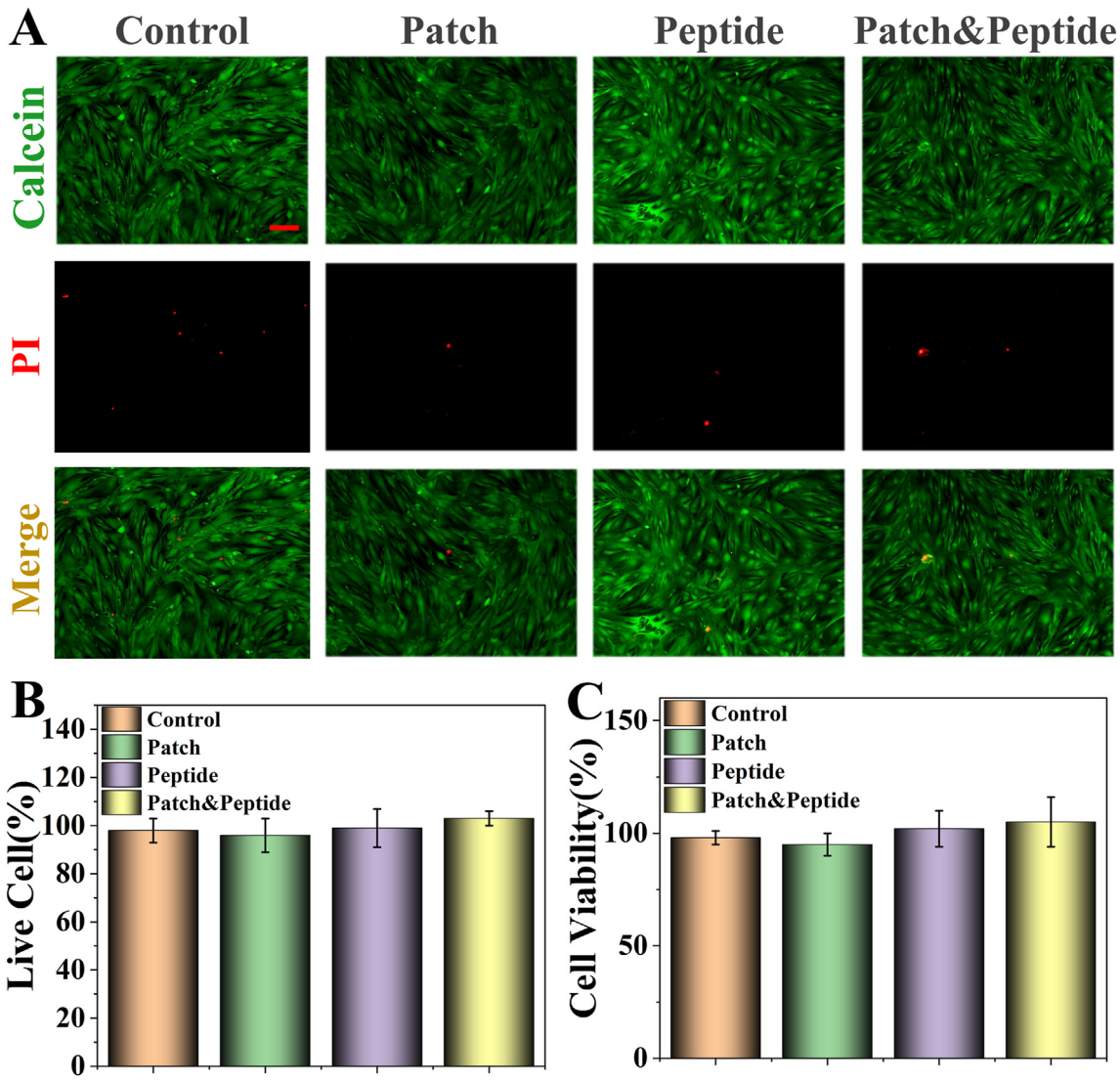

Fig. 4. Biocompatibility assays of the 3D-printed patches. (A) Live (green)/dead (red) staining of HDF cells on the different treatments; (B) the percentage of live cells; (C) Proliferation of HDF cells cultured directly on the different treatments detected by using the CCK-8 kit. The scale bars are 50 μm. Statistical analysis is shown on the bar graphs. Data are presented as the mean ± SD of the three independent experiments. There are not statistical differences between groups.

2.4. Wound healing assay and tubule formation assay in vitro

It has been previously reported that in endothelial cells QHREDGS promotes barrier functionality and cell metabolism, thereby inducing angiogenesis and skin wound healing [30]. An *in vitro* wound healing assay was performed to assess the migration of HDFs in different groups. Compared to the control group, the peptide group and patch & peptide group significantly enhanced HDF migration 48 h after scratching; however, the patch group was not affected (Fig. 5A, C). These results confirmed that QHREDGS induced the migration of HDFs, while 3D-printed patches alone did not affect cell migration in the wound healing assay. Next, we evaluated endothelial cell tube formation on Matrigel, a well-established *in vitro* angiogenesis assay that shows the ability of endothelial cells to form blood vessels as measured by tubule length after 48 h of different treatments. The tube-formation assay results showed that the peptide group and patch & peptide group had a significantly enhanced tubule network formation compared to the control group and patch group (Fig. 5B, D). At the same time, there were no differences between control and patch groups. These results indicated that the biological activity of QHREDGS was not affected by the 3D-printed patches, confirming its function to induce healing *in vitro*.

2.5. Wound closure study in vivo and histological analysis

To test the therapeutic efficacy of the 3D-printed patches in wound healing, a rat skin wound model was used and 1.5 cm diameter wounds were generated on the backs of SD rats. The rats were randomly divided into four groups and treated with PBS (control group), 3D-printed patches (patch group), QHREDGS solutions (peptide group), and 3D-printed peptide patches (patch & peptide group). The images of wounds on days 0, 3, 5, 7, and 9 were obtained and analyzed. Our results demonstrated that the patch & peptide group showed the fastest wound closure speed and the most efficient healing effect starting day 3, and an almost complete closure of the wound by day 9 (Fig. 6A, C). Wound healing was also facilitated in the peptide group compared with the control and patch groups; however, it was slower than in the patch & peptide group. To further confirm the repair ability of the patch & peptide group to promote wound healing, histological analysis was performed on skin tissues collected on day 9. The granulation tissue regenerated at the wound area after healing was analyzed by hematoxylin and eosin (HE) staining (Fig. 6B). In the peptide group and the patch & peptide group, those groups had higher relative tissue thickness. The patch & peptide group showed increased tissue thickness compared to all

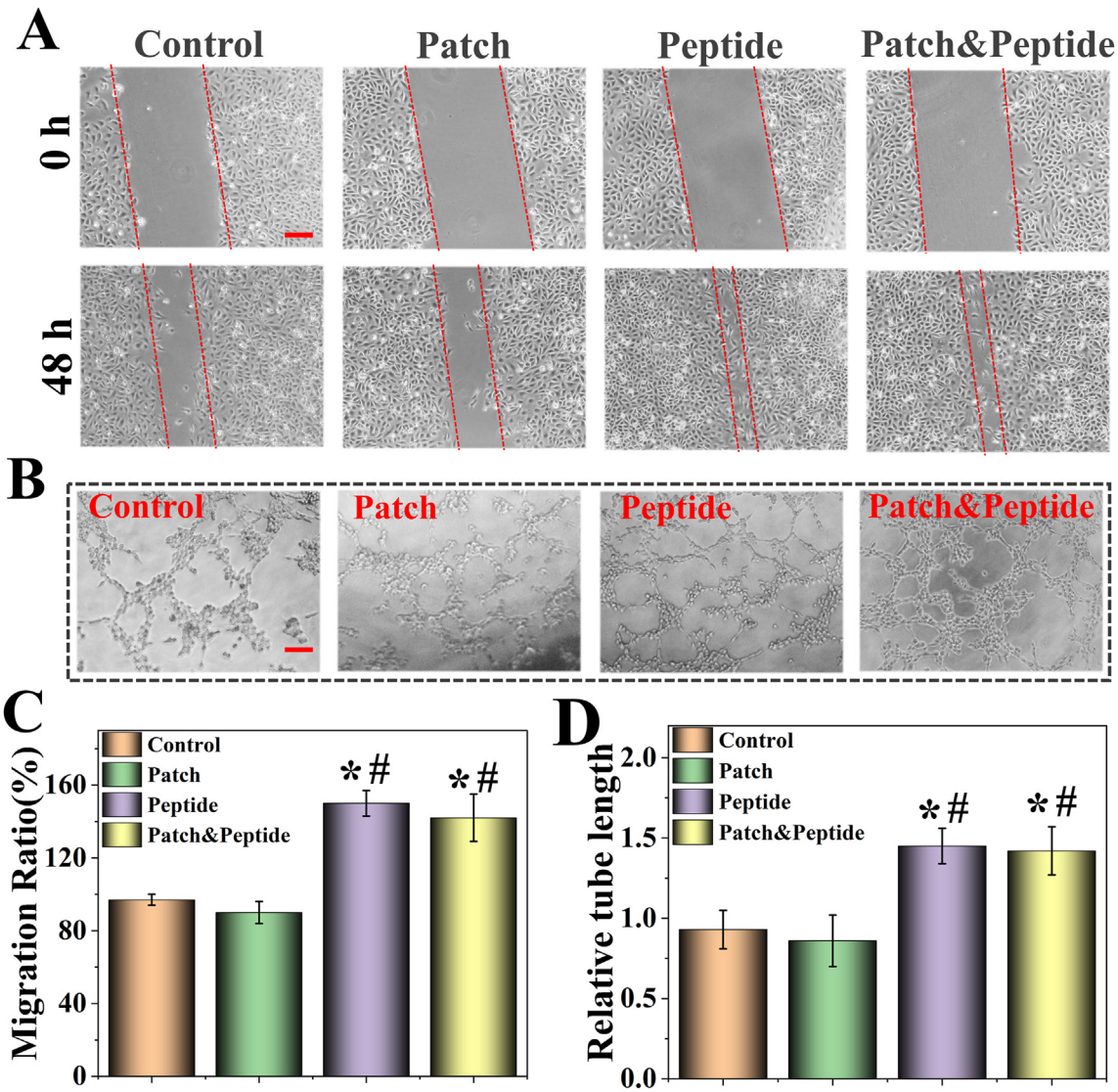

Fig. 5. Wound healing assays and tubule formation assays of the 3D-printed patches. (A) The cell migrations after HDF cells were scratched with different treatments. (B) The tube formation of HUVEC cells with different treatment; (C) quantitative analysis of cell migration with measurements of the gap size; (D) quantitative analysis of tubule formation assay results with measurements of the tube length. The scale bars are 100 μm. Statistical analysis is shown on the bar graphs. Data are presented as the mean ± SD of the three independent experiments. *P < 0.05 versus Control group; #P < 0.05 versus Patch group; & P < 0.05 versus Peptide group.

other groups (Fig. 6D), indicating that the 3D-printed peptide patches could be the more effective treatment of wound healing.

2.6. Hemolysis assay and biocompatibility in vivo

Next, we performed the hemolysis assay, a toxicity evaluation test to verify the biocompatibility of 3D-printed patches *in vivo* [31]. The results of the hemolysis tests are presented in Fig. S5. Our results showed that the supernatants of all four groups were clear at 0 h (Fig. S5A). Furthermore, after 5 h at 37 °C, there was no significant hemolysis and no difference between these four groups was observed (Fig. S5B). Next, we measured the absorbance of these supernatants at 570 nm, and our results showed that there were no differences between these four groups (Fig. S5C). Since the biocompatibility of the patches is one of the essential elements for using in clinic, the *in vivo* biocompatibility of 3D-printed patches was assessed by analyzing the major rat organs after 9-day treatment. The results showed that no damage to the heart, liver, spleen, lung, and kidney was induced by patches, peptide solutions, and peptide patches (Figure S6). Furthermore, no obvious inflammatory responses were observed in the samples from all four groups. Therefore, these 3D-printed patches showed favorable biocompatibility *in vivo*.

2.7. Expression analysis of proinflammatory factors

Inflammation is an important step during wound healing [32]. However, the healing process is slowed and the primary wound is further exacerbated when excessive inflammation is present [33]. Therefore, we evaluated the expression levels of two typical proinflammatory factors, interleukin-6 (IL-6) and tumor necrosis factor-α (TNF-α), on day 9 were using immunohistochemistry (Fig. 7A). Our results showed that high levels of IL-6 and TNF-α could be detected in the control group and patch group; however, there were no significant differences in cytokine levels between these two groups. At the same time, the levels of IL-6 and TNF-α were visibly lower in the patch & peptide group and peptide group, with the patch & peptide group showing the lowest expression levels of IL-6 and TNF-α (Fig. 7 B, C).

Finally, the remodeling of the extracellular matrix is the last stage of wound healing, and the deposition of collagen at the wound site is the

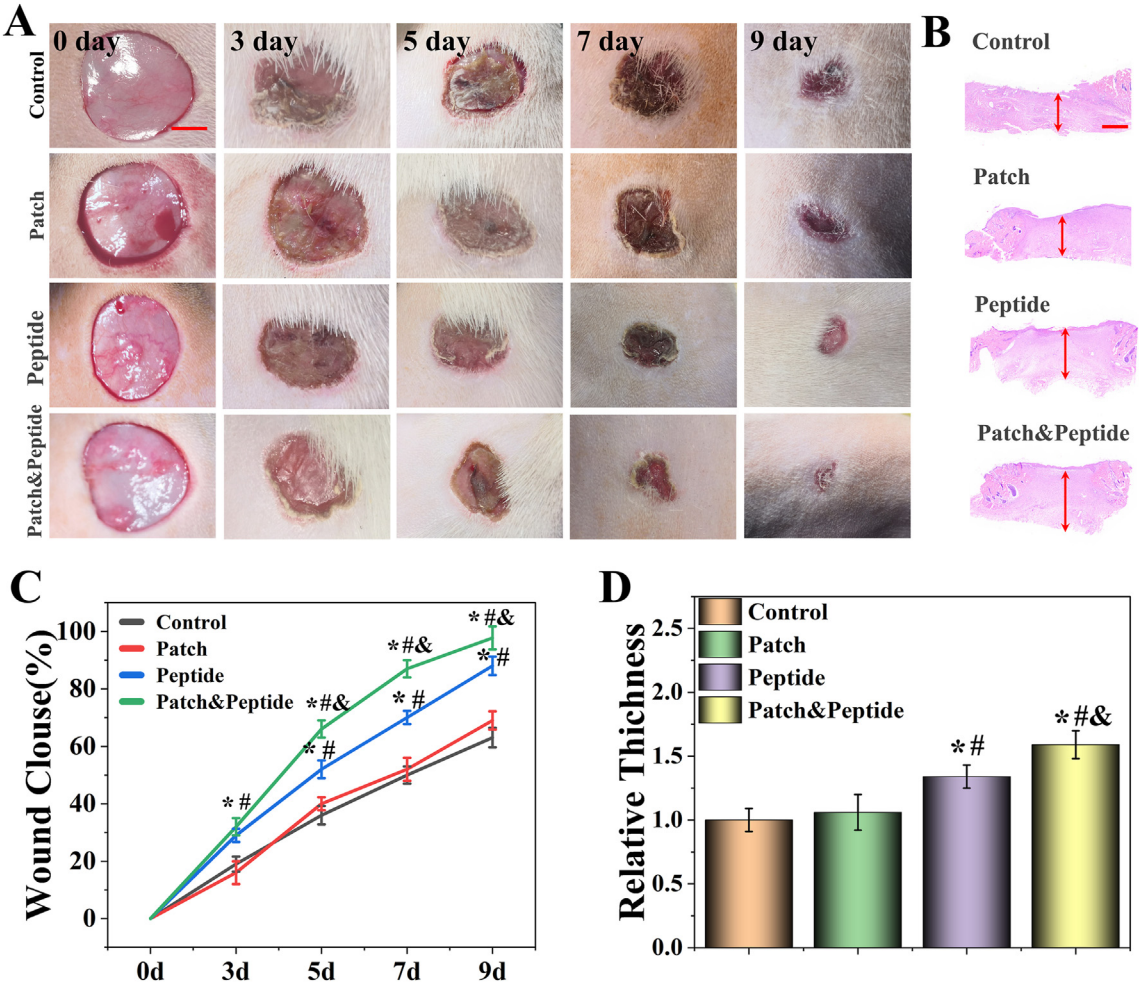

Fig. 6. (A) Representative images of the wounds from day 0 to day 9 with different treatment. (B) HE staining of wounds with different treatment at day 9; (C) wound repair rate characterized by wound area from day 0 to day 9; (D) quantitative analysis of granulation tissue thickness at day 9. The scale bars are 5 mm in (A) and 400 μm in (B). Statistical analysis is shown on the bar graphs. Data are presented as the mean ± SD of the five independent experiments. *P < 0.05 versus Control group; #P < 0.05 versus Patch group; & P < 0.05 versus Peptide group.

key feature of skin remodeling [34]. Therefore, we evaluated collagen deposition in all groups using Masson's trichrome staining (Fig. 7A). Our results showed that the patch & peptide group showed the highest level of collagen deposition compared with other groups (Fig. 7D), consistent with the results of wound closure experiment.

2.8. Neovascularization marker protein expression analysis

Neovascularization plays an important role in wound healing by providing oxygen, nutrients, and bioactive factors to the wound sites [35]. CD31 and α-smooth muscle actin (α-SMA) are the markers of vascular endothelial cells and vascular smooth muscle cells, respectively [36]. To evaluate neovascularization at the wound sites, we assessed the protein expression of CD31 and α-SMA using immunofluorescent double-staining (Fig. 8A). Our results showed that the patch & peptide group had the highest relative vessel density (double CD31 and α-SMA staining) compared to other groups, indicating the highest number of vascular structures at the wound site (Fig. 8B). In addition, the peptide group also had higher expression levels of CD31 and α-SMA than control and patch groups, but lower than those in the patch & peptide group. Our results suggest that the synergy between GelMA/HAMA and QHREDGS allowed efficient vascular reconstruction, with QHREDGS playing a major role in increasing the rate of angiogenesis. Collectively, these results further indicate that 3D-printed peptide patch promote vessel formation and wound repair *in vivo*.

3. Materials and methods

3.1. Materials

QHREDGS and FITC-peptide were bought from Hefei Synthbio Co., Ltd. (Hefei, China). GelMA and HAMA were purchased from Engineering for Life Co., Ltd (Suzhou, China). HDF cells and human umbilical vein endothelial cells (HUVECs) were purchased from Cyagen Biosciences (Guangzhou, China). Fetal bovine serum (FBS) and F12/Dulbecco's modified Eagle's medium (F12/DMEM) were obtained from HyClone (Logan, Utah, USA). Calcein-AM/PI staining kit was purchased from Invitrogen (Shanghai, China). Growth factor-reduced Matrigel was purchased from BD Bioscience (Shanghai, China). Collagenase II was obtained from Sigma-Aldrich (MO, USA). CCK 8 was purchased from Keygen Biotech Co. (Nanjing, China). Male SD rats (6–8-week-old) were provided by hunan sja laboratory animal co., ltd. (Changsha, China). All of the rats were treated strictly according to the guidelines of the Animal Ethic Committee of Jiujiang University.

3.2. Preparation of 3D-printed patches

The printable ink was prepared by mixing the GelMA (15%, w/v), HAMA (5%, w/v), and HMPP (1%, w/v) were dissolved in 2% sodium alginate solution. The image of GelMA/HAMA hydrogel formation before and after UV light were shown in Supplementary Fig. S7. The patch was

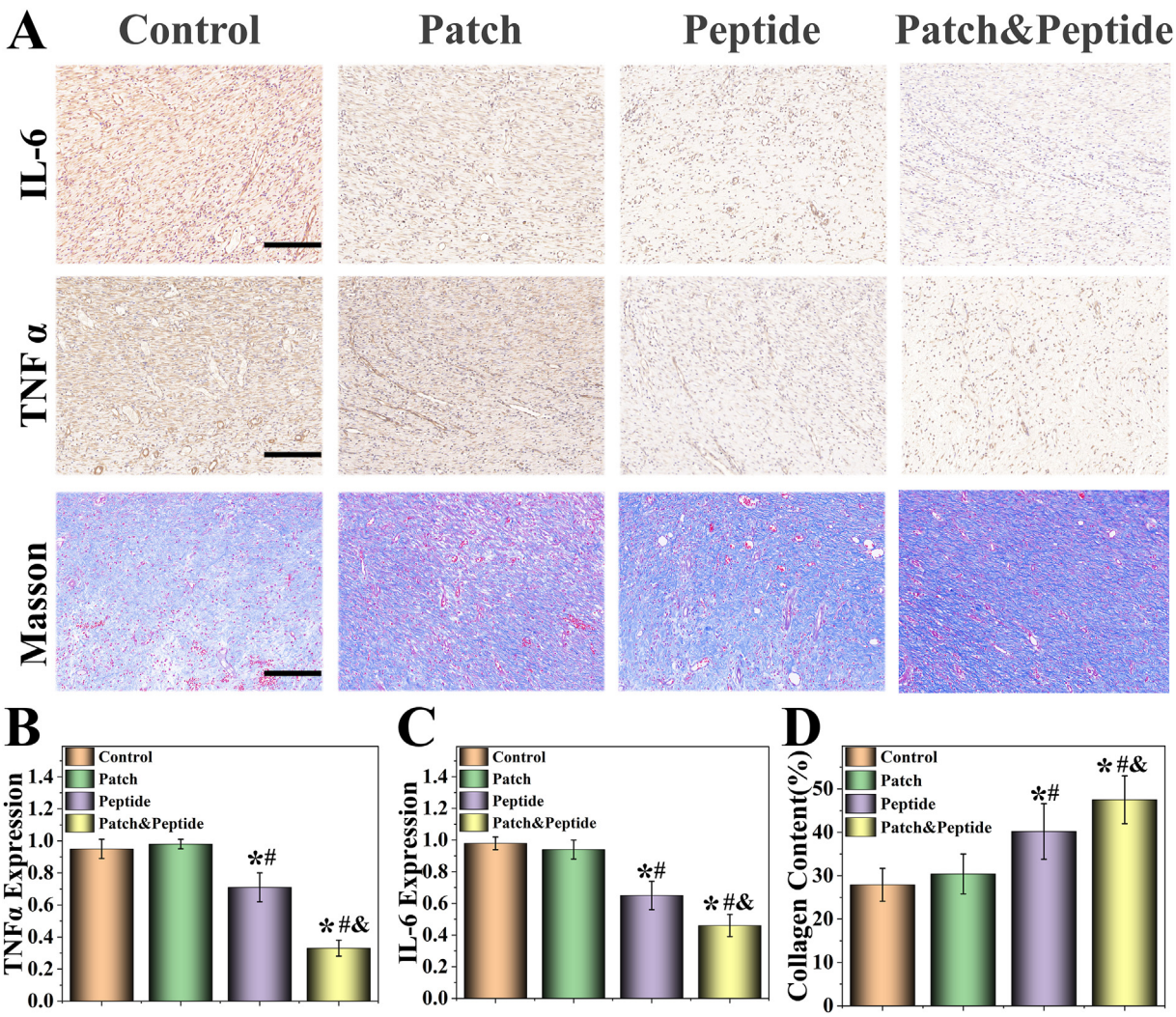

Fig. 7. Characterization of proinflammatory factors, collagen deposition. (A) Masson's trichrome staining, immunostaining of IL-6 and TNFα at granulation tissues in different groups; (B–D) Representative (B) IL-6, (C) TNFα, and (D) collagen deposition analysis in different groups after treatment. The scale bars are 200 μm. Statistical analysis is shown on the bar graphs. Data are presented as the mean ± SD of the five independent experiments. *P < 0.05 versus Control group; #P < 0.05 versus Patch group; & P < 0.05 versus Peptide group.

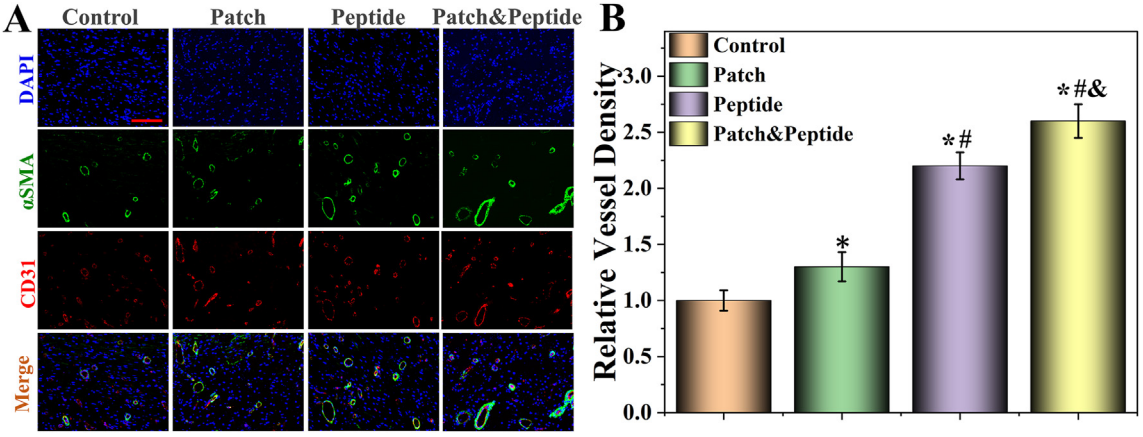

Fig. 8. Characterization of neovascularization. (A) The fluorescent images of the immunostaining of αSMA (green) and CD31 (red); (B) the analysis of vessel density. The scale bars are 200 μm. Statistical analysis is shown on the bar graphs. Data are presented as the mean ± SD of the five independent experiments. *P < 0.05 versus Control group; #P < 0.05 versus Patch group; & P < 0.05 versus Peptide group.

made by a modified 3D printer (Bio-Architect, Regenovo, China). The bioink was carefully loaded into a 5 ml of extrusion syringe, which was fixed on the conveyor for extrusion through 20G (600 μm, thick filaments) or 23G (300 μm, thin filaments) flat tip needle. These 3D patches model with dimensions of approximately 15 mm diameter were designed. The temperature of the dispenser and bed were 30 °C and 10 °C, respectively. After the hydrogel patches were printed, UV (365 nm) irradiation with an intensity of 10 mW/cm^2 for 5 min was applied to cross-link the samples. The light photocuring efficiency of 3D-printed patches was verified by exposure or shading UV light irradiation (Fig. S8).

3.3. Characterization

The pictures of 3D-printed patches were taken with a light microscope (Olympus BX51, Japan) equipped with a color charge-coupled device (CCD) camera (Media Cybernetics Evolution MP 5.0). Scanning electron microscopy (SEM) imaging and analysis were conducted to evaluate the porosity of the crosslinked composite hydrogels. The hydrogel was freeze-died for 24 h at −55 °C at 6.5 hPa before measurements, using lyophilizer Heto PowerDry PL3000 (Thermo Scientific, USA). Freeze-dried hydrogel samples were sputtered with gold to improve conductivity. Finally, SEM images were obtained using SEM (Hitachi, S–300 N).

3.4. Biodegradability test

The biodegradability of 3D-printed patches was determined using a collagenase type II solution by mimicking the physiological environments, as previously described [26]. In briefly, the weight of the freeze-dried hydrogel was denoted as W0. The hydrogel patches were then soaked in 2 U/ml of collagenase II in a 37 °C, constant temperature water bath, and new collagenase II was replaced every day. When taken out at different time points, the weight after freeze-drying was recorded as Wt. The percent degradation rate (WD) of the sample was denoted as WD = Wt/W0 × 100%.

3.5. Generation of 3D-printed peptide patches

3D-printed patches were chemically modified with QHREDGS peptide as previously reported [37]. The synthesis procedures of 3D-printed peptide patches were described in Fig. S9. Briefly, 3D-printed GelMA/-HAMA patches were soaked in 10 ml of MES buffer (pH = 6). Then, EDC and NHS were added successively and activated at 37 °C for 15 min. Next, 100 mg of QHREDGS was added and incubated at 37 °C for 12 h. The patches were washed 3 times and freeze-dried for 48 h.

3.6. Peptide release studies

To test the peptide release rate of 3D patches, FITC-peptide was used as a marker. As the above method, the 3D-printed thin or thick filaments patches chemically conjugated by FITC-peptide under the same reaction conditions. Moreover, as a physical absorption group, the lyophilized 3D-printed thin or thick filaments patches were submerged in 10 mg/ml FITC-peptide solutions for 12 h. The patches were washed 3 times. Then, these patches were freeze-dried for 48 h and collected. Finally, Lyophilized patches were kept in 100 ml PBS (pH 7.4) and was equilibrated at 37 °C ± 0.5 °C with shaking at 100 rpm. Fluorescence images of the patches were captured after every day. Relative fluorescence intensity (%) was expressed as a ratio of the fluorescence intensity at a particular time normalized to the initial fluorescence intensity.

3.7. Cell culture and treatment

HDF cells and HUVECs were cultured in DMEM/F12 with 10% v/v FBS and 1% v/v antibiotic-antimycotic solution. Cells were maintained at standard conditions in a humidified atmosphere incubator at 37 °C with 5% CO_2. For treatment, the cells were divided into four groups: control, patch, peptide and patch & peptide groups. Cells were treated with PBS (control group), the soaked solution of 3D-printed patches (patch group), QHREDGS solution (peptide group), and the soaked solution of 3D-printed peptide patches (patch & peptide group) for 48 h in the same volume. The QHREDGS concentration of peptide group was selected to be consistent with the QHREDGS concentration of the soaking solution of peptide patches for 48 h. The detailed methods are described in Supplementary methods.

3.8. Biocompatibility analysis in vitro

Cell viability was determined via a Calcein-AM/PI staining according to instructions. Briefly, The HDF cells samples were incubated with a 400 μl staining solution containing 2 μl/ml Calcein-AM and 4 μl/ml PI for 1 h following treated as described above. Then, the staining solutions were removed, and the cells were washed twice using PBS. Finally, randomly selected areas of each sample were observed and photographed by fluorescence inverted microscope (Olympus CKx53, Japan). Live and dead cell numbers were counted using ImageJ (Image J 1.48v, NIH, USA) and the percentage of live cell was quantified as the number of live cells divided by the total cell number. As for the proliferation analysis, a CCK-8 assay was performed to evaluate the survival of HDF cells. Briefly, followed different treatment, cells were incubated with 10 μl CCK-8 solution for an additional 2 h at 37°C, and the absorbance value was measured at a wavelength of 450 nm using a microplate reader. Cell viability was calculated as follows: Cell viability (%) = (OD treatment/OD control) × 100%.

3.9. Wound healing assays

A scratch assay was performed on HUVECs grown to confluency. Briefly, HUVECs were seeded at a density of 1 × 10^6 cells/well in 6-well plates for 24 h. Cell layers were scratched using a 200-μl pipette tip to form a wound-like gap. The cells were treated in accordance with the above groupings for 48 h. And images were captured at 0 and 48 h. The rate of cell migration was expressed as surface area (μm^2) covered by migrating cells divided by time. To establish the area into which the cells had migrated at each time point, the area of the wound at each time point was subtracted from the initial area of the wound. ImageJ was used to determine the area of the wound. The migration rate (%) = (scratch distance-distance after growing)/scratch distance.

3.10. Tubule formation assays

HUVECs were used for the tube-formation test *in vitro*. Briefly, the cells were treated in accordance with the above groupings for 48 h. The HUVECs (~6 × 10^4/ml) of different groups were seeded in a 24-well plates coated with growth factor-reduced Matrigel. After 8 h of culture, the cells were observed under the light microscope. The total tube length was quantified by the ImageJ software.

3.11. Hemolysis assay

The hemolysis test was used to evaluate the safety of patches. Fresh rat blood (10 ml) was collected, and the fibrinogen fraction was removed by stirring with a glass rod. The erythrocytes in the defibrinated blood were washed three times with 10 ml of PBS. Each wash step included centrifugation at 2500 rpm for 5 min, followed by removal of the supernatant. A 2% (v/v) erythrocyte suspension was prepared by diluting the erythrocytes with PBS. Four glass test tubes containing 5 ml of 2% (v/v) erythrocyte suspension were added and mixed individually with the PBS, 3D-printed patches, QHREDGS solution, and 3D-printed peptide patches, and allowed to stand for 5 h at 37°C. Furthermore, the super-

natant was collected by centrifuging the samples, and its absorbance was recorded at 570 nm using a microplate reader (Biotek, ELX800, USA).

3.12. Animal study

All the SD rats were fasted overnight before use. To prepare the skin wound model, the rats were anesthetized by intraperitoneal injection the mixture of xylazine (5 mg/kg body weight) and ketamine (50 mg/kg body weight). Afterwards, the wounds were formed by removing circular skins with a diameter of about 1.5 cm on the back of these animals, and the rats were divided into four groups randomly (n = 5 for each group). Then the wounds were treated with the PBS, 3D-printed patches, QHREDGS solution, and 3D-printed peptide patches as control, patch, peptide, and patch & peptide groups, respectively. The peptide concentration of peptide solutions was selected to be consistent with the peptide concentration of peptide patches. The detailed methods are described in Supplementary methods. When the rats recovered from anesthesia, they were put back into separated cages with sufficient water and food. The wounds were observed and photographed on different days. The wound area was calculated from measurements taken on days 3, 5, 7, and 9 after injury using ImageJ software. The wound healing rate was calculated as follows: The wound closure rate (%) = (Area-of initial wound–Area of residual wound)/Area of initial wound × 100%. After 9 days, the rats were sacrificed, and the regenerated tissues at the wound sites were excised for the histological analysis. In order to study the biocompatibility *in vivo*, the surrounding tissues were surgically removed and subjected to HE staining.

3.13. Histology, immunohistochemistry and immunofluorescence staining

The samples were embedded in paraffin after dehydrated with a series of gradient ethanol. Then the embedded samples were cut into serial sections with a thickness of 5 μm by using a microtome. The sections were used for HE staining, Masson's trichrome staining to evaluate epithelization and collagen deposition. IL-6 and TNF-α staining were used for immunohistochemistry to evaluate the inflammation. Immunofluorescence staining by primary antibodies CD31 and α-SMA were utilized for neovascularization analysis.

3.14. Statistical analyses

Statistical analyses were analyzed using GraphPad Prism (GraphPad Software, La Jolla, CA). All results were expressed as mean values ± standard deviations (SD). One-way analysis of variance and Tukey's multiple comparison posttest were used. Differences were considered significant for $p < 0.05$.

4. Conclusions

In summary, we developed a novel angiogenic 3D-printed peptide patches for wound healing. The 3D bioprinting is applicated to overcome the limitations due to its ability for precise multimaterial and multiscale fabrication. The patches based on the hydrogel of a proportional mixing GelMA/HAMA, which is significant to mimic the cell compositions and extracellular matrix of the skin tissues. QHREDGS as a novel pro-angiogenic peptide, the treatment effect of its 3D printed hydrogels patches on skin wound was first verified. Moreover, covalent conjugated QHREDGS are effective in promoting skin wound healing by prolonging the peptide release in 3D-printed patches. Therefore, these unique features make the 3D-printed peptide patches a potential measure for skin wound treatment.

Credit author statement

GP. Guan: Investigation, Writing- Original draft preparation. QZ. Lv: Project administration, Writing- Reviewing and Editing. SY. Liu: Investigation, Software, Visualization. ZZ. Jiang: Investigation, Data curation. CX. Zhou: Resources, Supervision, conceptualization. WF. Liao: Conceptualization, Methodology, Validation.

Data availability statement

Data availability may be granted by contacting the corresponding author.

Declaration of competing interest

The authors declare that they have no known competing financial interests or personal relationships that could have appeared to influence the work reported in this paper.

Acknowledgements

This study was not supported by external funds. We would like to thank Dr. Puhua Zhang for his critical suggestions and proof reading on the manuscript.

Appendix A. Supplementary data

Supplementary data to this article can be found online at https://doi.org/10.1016/j.mtbio.2021.100188.

References

[1] R. Yi, The Skin (ny) on regenerating the largest organ to save a patient's life, Cell. Stem. Cell. 22 (1) (2018) 14–15.
[2] M. Aragona, S. Dekoninck, S. Rulands, S. Lenglez, G. Mascré, B.D. Simons, C. Blanpain, Defining stem cell dynamics and migration during wound healing in mouse skin epidermis, Nat. Commun. 8 (2017) 14684.
[3] R. Zhao, H. Liang, E. Clarke, C. Jackson, M. Xue, Inflammation in chronic wounds, Int. J. Mol. Sci. 17 (12) (2016) 2085.
[4] Sheila MacNeil, Progress and opportunities for tissue-engineered skin, Nature 445 (7130) (2007) 874–880.
[5] C.E. Fife, M.J. Carter, D. Walker, B. Thomson, Wound care outcomes and associated cost among patients treated in us outpatient wound centers: data from the us wound registry, Wounds 24 (1) (2012) 10–17.
[6] E. Ikeda, R. Morita, K. Nakao, K. Ishida, T. Nakamura, T. Takano-Yamamoto, M. Ogawa, M. Mizuno, S. Kasugai, T. Tsuji, Fully functional bioengineered tooth replacement as an organ replacement therapy, P. Natl. Acad. Sci. USA. 106 (32) (2009) 13475–13480.
[7] J. Ni, H. Ling, S. Zhang, et al., Three-dimensional printing of metals for biomedical applications, Mater. Today. Bio. 3 (2019) 100024.
[8] A.A. Zadpoor, J. Malda, Additive manufacturing of biomaterials, tissues, and organs, Ann. Biomed. Eng. 45 (1) (2017) 1–11.
[9] A. Smandri, A. Nordin, N.M. Hwei, K.Y. Chin, I.A. Aziz, M.B. Fauzi, Natural 3D-Printed Bioinks for Skin Regeneration and wound healing: a systematic review, Polymers-basel 12 (8) (2020) 1782.
[10] K. Yue, T.D. Santiago, M.M. Alvarez, A. Tamayol, N. Annabi, A. Khademhosseini, Synthesis, properties, and biomedical applications of gelatin methacryloyl (GelMA) hydrogels, Biomaterials 73 (2015) 254–271.
[11] V. Mouser, A. Abbadessa, R. Levato, W.E. Hennink, T. Vermonden, D. Gawlitta, J. Malda, Development of a thermosensitive HAMA-containing bio-ink for the fabrication of composite cartilage repair constructs, Biofabrication 9 (1) (2017), 015026.
[12] L. Lei, Q. Lv, Y. Jin, H. An, Z. Shi, G. Hu, Y. Yang, X. Wang, L. Yang, Angiogenic microspheres for the treatment of a thin endometrium, ACS Biomater. Sci. Eng. 7 (10) (2021) 4914–4920.
[13] K. Moschouris, N. Firoozi, Y. Kang, The application of cell sheet engineering in the vascularization of tissue regeneration, Regen. Med. 11 (6) (2016) 559–570.
[14] M. Hajimiri, S. Shahverdi, G. Kamalinia, R. Dinarvand, Growth factor conjugation: strategies and applications, J. Biomed. Mater. Res. 103 (2) (2015) 819–838.
[15] R. Patricia, B.F. bienne, D. Guila, Re-epithelialization of adult skin wounds: cellular mechanisms and therapeutic strategies, Adv. Drug Deliv. Rev. 146 (2019) 344–365.
[16] S. Vignesh, S. Deepthi, A. Sivashanmugam, S. Srinivasan, R. Jayakumar, Pro-angiogenic molecules for therapeutic angiogenesis, Curr. Med. Chem. 24 (31) (2017) 3413.
[17] M. Erak, K. Bellmann-Sickert, S. Els-Heindl, A.G. Beck-Sickinger, Peptide chemistry toolbox – transforming natural peptides into peptide therapeutics, Bioorg. Med. Chem. 26 (10) (2018) 2759–2765.
[18] A.J. Kastin, W. Pan, Concepts for biologically active peptides, Curr. Pharmaceut. Des. 16 (30) (2010) 3390–3400.
[19] L.T. Dang, N.T. Feric, C. Laschinger, W.Y. Chang, B. Zhang, G.A. Wood, W.L. Stanford, M. Radisic, Inhibition of apoptosis in human induced pluripotent

stem cells during expansion in a defined culture using angiopoietin-1 derived peptide QHREDGS, Biomaterials 35 (27) (2014) 7786–7799.
[20] V.M. Ahrens, K. Bellmann-Sickert, A.G. Beck-Sickinger, Peptides and peptide conjugates: therapeutics on the upward path, Future, Med. Chem. 4 (12) (2012) 1567–1586.
[21] M.J. Jang, S.K. Bae, Y.S. Jung, J.C. Kim, J. Kim, S.K. Park, J.S. Suh, S.J. Yi, S.H. An, J.O. Lim, Enhanced wound healing using a 3D printed VEGF-mimicking peptide incorporated hydrogel patch in a pig model, Biomed. Mater. 16 (4) (2021) 10.
[22] B. Chu, J. He, Z. Wang, L.L. Liu, M. Tu, Proangiogenic peptide nanofiber hydrogel/3D printed scaffold for dermal regeneration, Chem. Eng. J. (2020) 128146.
[23] P. Xu, J. Guan, Y. Chen, H. Xiao, T. Yang, H. Sun, N. Wu, C. Zhang, Y. Mao, Stiffness of photocrosslinkable gelatin hydrogel influences nucleus pulposus cell properties in vitro, J. Cell Mol. Med. 25 (2) (2021) 880–891.
[24] L. Wang, Y. Li, B. Chen, S. Liu, M. Li, L. Zheng, P. Wang, T.J. Lu, F. Xu, Patterning cellular alignment through stretching hydrogels with programmable strain gradients, ACS Appl. Mater. Interfaces 7 (27) (2015) 15088–15097.
[25] Z. Wang, H. Kumar, Z. Tian, X. Jin, J.F. Holzman, F. Menard, K. Kim, Visible light photoinitiation of cell-adhesive gelatin methacryloyl hydrogels for stereolithography 3D bioprinting, ACS Appl. Mater. Interfaces 10 (32) (2018) 26859–26869.
[26] K. Rahali, G. Ben Messaoud, C.J. Kahn, L. Sanchez-Gonzalez, M. Kaci, F. Cleymand, S. Fleutot, M. Linder, S. Desobry, E. Arab-Tehrany, Synthesis and characterization of nanofunctionalized gelatin methacrylate hydrogels, Int. J. Mol. Sci. 18 (12) (2017) 2675.
[27] C.T. McKee, J.A. Last, P. Russell, C.J. Murphy, Indentation versus tensile measurements of Young's modulus for soft biological tissues, Tissue Eng. B Rev. 17 (3) (2011) 155–164.
[28] B. Velasco-Rodriguez, T. Diaz-Vidal, L.C. Rosales-Rivera, C.A. García-González, C. Alvarez-Lorenzo, A. Al-Modlej, V. Domínguez-Arca, G. Prieto, S. Barbosa, J.F.A. Soltero Martínez, Hybrid methacrylated gelatin and hyaluronic acid hydrogel scaffolds. preparation and systematic characterization for prospective tissue engineering applications, Int. J. Mol. Sci. 22 (13) (2021) 6758.
[29] S.D. Girolamo, C. Puorger, G. Lipps, Stable and selective permeable hydrogel microcapsules for high-throughput cell cultivation and enzymatic analysis, Microb. Cell Factories 19 (1) (2020) 1–13.
[30] J.W. Miklas, S.M. Dallabrida, L.A. Reis, I. Nesreen, R. Maria, R. Milica, M.A. Deli, QHREDGS enhances tube formation, metabolism and survival of endothelial cells in collagen-chitosan hydrogels, PLoS One 8 (8) (2013), e72956.
[31] L.C.L. Haynes, Impacts of mesoporous silica nanoparticle size, pore ordering, and pore integrity on hemolytic activity, J. Am. Chem. Soc. 132 (13) (2010) 4834.
[32] W. Wang, X. Yan, Y. Lin, H. Ge, Q. Tan, Wnt7a promotes wound healing by regulation of angiogenesis and inflammation: issues on diabetes and obesity, J. Dermatol. Sci. 91 (2) (2018) 124–133.
[33] T. Hess, Cathy, Checklist for factors affecting wound healing, Adv. Skin Wound Care 24 (4) (2011) 192.
[34] L. Lei, Y. Zhu, X. Qin, S. Chai, G. Liu, W. Su, Q. Lv, D. Li, Magnetic biohybrid microspheres for protein purification and chronic wound healing in diabetic mice, Chem. Eng. J. 425 (5) (2021) 130671.
[35] P.S. Briquez, L.E. Clegg, M.M. Martino, F.M. Gabhann, J.A. Hubbell, Design principles for therapeutic angiogenic materials, Nat. Rev. Mater. 1 (1) (2016) 15006.
[36] J. Wang, D. Xu, J. Cui, S. Wang, W. Bai, A new approach for examining the neurovascular structure with phalloidin and calcitonin gene-related peptide in the rat cranial dura mater, J. Mol. Histol. 51 (5) (2020) 541–548.
[37] J. Bian, F. Cai, H. Chen, Z. Tang, L. Chen, Modulation of local overactive inflammation via injectable hydrogel microspheres, Nano Lett. 21 (6) (2021) 2690–2698.